

See discussions, stats, and author profiles for this publication at: <https://www.researchgate.net/publication/51161909>

Redox-Promoting Protein Motions in Rubredoxin

ARTICLE *in* THE JOURNAL OF PHYSICAL CHEMISTRY B · MAY 2011

Impact Factor: 3.3 · DOI: 10.1021/jp201346x · Source: PubMed

CITATIONS

5

READS

24

8 AUTHORS, INCLUDING:



[Jose Borreguero](#)

Oak Ridge National Laboratory

24 PUBLICATIONS 825 CITATIONS

[SEE PROFILE](#)



[Flora Meilleur](#)

North Carolina State University

53 PUBLICATIONS 563 CITATIONS

[SEE PROFILE](#)



[Kevin L Weiss](#)

Oak Ridge National Laboratory

40 PUBLICATIONS 419 CITATIONS

[SEE PROFILE](#)



[Craig Martin Brown](#)

National Institute of Standards and Technol...

157 PUBLICATIONS 5,850 CITATIONS

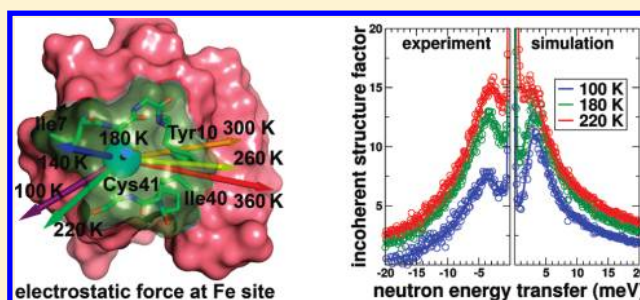
[SEE PROFILE](#)

Redox-Promoting Protein Motions in Rubredoxin

Jose M. Borreguero,^{*,†} Junhong He,[†] F. Meilleur,^{†,‡} Kevin L. Weiss,[†] Craig M. Brown,[§] Dean A. Myles,[†] Kenneth W. Herwig,^{*,†} and Pratul K. Agarwal[⊥][†]Neutron Scattering Science Division, Oak Ridge National Laboratory, Oak Ridge, Tennessee 37831, United States[‡]Molecular and Structural Biochemistry Department, North Carolina State University, Raleigh, North Carolina 27695, United States[§]National Institute of Standards and Technology, Center for Neutron Research, Gaithersburg, Maryland 20899, United States[⊥]Computer Science and Mathematics Division, Oak Ridge National Laboratory, Oak Ridge, Tennessee 37831, United States

S Supporting Information

ABSTRACT: Proteins are dynamic objects, constantly undergoing conformational fluctuations, yet the linkage between internal protein motion and function is widely debated. This study reports on the characterization of temperature-activated collective and individual atomic motions of oxidized rubredoxin, a small 53 residue protein from thermophilic *Pyrococcus furiosus* (RdPf). Computational modeling allows detailed investigations of protein motions as a function of temperature, and neutron scattering experiments are used to compare to computational results. Just above the dynamical transition temperature which marks the onset of significant anharmonic motions of the protein, the computational simulations show both a significant reorientation of the average electrostatic force experienced by the coordinated Fe^{3+} ion and a dramatic rise in its strength. At higher temperatures, additional anharmonic modes become activated and dominate the electrostatic fluctuations experienced by the ion. At 360 K, close to the optimal growth temperature of *P. furiosus*, simulations show that three anharmonic modes including motions of two conserved residues located at the protein active site (Ile7 and Ile40) give rise to the majority of the electrostatic fluctuations experienced by the Fe^{3+} ion. The motions of these residues undergo displacements which may facilitate solvent access to the ion.



■ INTRODUCTION

An integrated view of protein structure, flexibility, and function is emerging.^{1–5} Increasing evidence continues to indicate that proteins should not be regarded as static objects, but rather as intrinsically flexible molecules constantly sampling the kinetically accessible part of their energy landscape.³ However, the role of internal protein motions in facilitating protein function is a topic of ongoing debate.^{6,7} Important insights into catalysis have been gained by identifying collective motions linking the flexibility of surface loops and reaction-promoting local motions at the active site of several enzymes.^{1,8,9} Moreover, these collective motions have been discovered to arise from conserved aspects of the molecular architecture, lending evidence that they have an important role in protein function.¹

Elucidating the relationship between protein flexibility and function requires a detailed identification and characterization of protein motion over a wide range of time and length scales.^{4,9} This is a significant challenge because protein motions occur over a broad range of time scales, arguably, at least 12 orders of magnitude (10^{-15} to 10^{-3} s), making them difficult to characterize using any single experimental technique.¹⁰ Computational modeling provides both a bridge that can unite disparate experimental measurements (over a wide range of time scales)

and a framework for their interpretation, while the experimental data validates the theoretical methodology. Validated models can then be used to extend our understanding beyond questions that can be readily investigated by experiment and aid in the design of new measurement strategies. Complementing experiments with computational modeling has previously allowed characterization of fast motions (10^{-14} to 10^{-9} s) within individual residues as well as slow conformational fluctuations ($>10^{-6}$ s) of entire proteins^{11,12} and is the approach followed in this investigation.

Incoherent quasi-elastic neutron scattering (QENS) is a promising experimental technique to investigate protein motions in the 10^{-12} to 10^{-9} s time-scale range. The single proton in the hydrogen atom nucleus has a very strong interaction with the neutron resulting in a scattering probability for hydrogen that is much higher than that for other atoms found in proteins.^{13,14} Thus, QENS is highly sensitive to the motion of individual hydrogen atoms that are distributed throughout the protein, with much less sensitivity to the remaining protein atoms. In addition, the scattering lengths of the proton combine in such a fashion as

Received: February 10, 2011

Revised: May 2, 2011

to produce a largely incoherent interaction with the neutron whose practical implication is that only the self-term of the dynamic structure factor needs to be considered (see for example, eq S1 in SI) simplifying interpretation of the experimental data. The length scales probed by QENS typically range from around 0.3 to 3 nm which match the relevant length scales for protein side chain motion over the accessible time range.

The combination of molecular dynamics (MD) simulations and QENS provide a powerful methodology for atomic level characterization of protein internal motions. The link between QENS and MD simulations is direct as QENS measures the dynamic structure factor, a quantity which can be readily calculated from the atomic trajectories produced in the simulation. QENS has been applied to the study of proteins and synthetic systems of biological relevance^{15–18} with much recent interest centered on the so-called dynamical transition and the interplay of the dynamics of hydration water with that of the protein.^{19–22} Observed universally in hydrated proteins by QENS and other experimental techniques,²³ the dynamical transition temperature (T_{DT}) marks the onset of anharmonic motions, particularly diffusive motions of the protein side chains.²⁴ At low temperatures and on the time scale of the experiment, the environment of each atom can be considered as “frozen” for all purposes. In this environment, neighboring atoms exert harmonic forces, and atoms in the protein undergo vibrational motions. Some of these vibrational motions, or modes, involve many atoms undergoing coherent displacements from their corresponding average positions. Apart from methyl group rotations, proteins exhibit mostly harmonic, vibrational motion at temperatures below T_{DT} .²⁵ At temperatures above T_{DT} , the environment of each atom changes in the time scale of the experiment due to finite displacements of the neighboring atoms. Forces resulting from non-bonding interactions from these neighboring atoms lose the coherence that was present at low temperatures. In this regime, the resulting net force acting on each atom can be considered semirandom, giving rise to diffusion. Nevertheless, each atom of the protein is prevented from diffusing freely because it is covalently bonded to other atoms of the protein, effectively confining the atom to diffuse within a finite volume. In several proteins, the change in dynamic behavior around T_{DT} has been correlated with the onset of specific activity, lending evidence for a link between dynamics and function.^{26,27}

Occurring on shorter time scales than probed by QENS is the occurrence of a *boson peak* in the low temperature protein dynamics which can be measured by inelastic neutron scattering^{28–30} (INS) and other techniques.³¹ The boson peak has also been observed in glasses^{32,33} and amorphous solids^{34,35} as a local maximum of the dynamic structure factor in the 2–5 meV energy transfer range. The boson peak is essentially an excess of low energy excitations beyond what is observed in crystalline materials and a ubiquitous phenomenon of systems endowed with a rugged energy landscape, and several hypotheses have been formulated to explain its origin.^{30,36,37} One hypothesis states that the boson peak arises in proteins from collective motions of atoms with damped resonances at frequencies in the acoustic range.³⁰ As the temperature is increased, the boson peak weakens and eventually disappears as it is replaced or masked by the rise of quasielastic scattering extending into the same energy transfer range. It is intriguing to postulate that those residues whose collective motions make the strongest contributions to the low temperature boson peak, may also, at higher temperatures,

participate in diffusive motions relevant to function and in the flow of energy from one part of the protein to another. Note that it has been hypothesized that some enzymes channel thermal energy fluctuations of the solvent toward the active site thereby promoting a motion integral to function.¹

The protein investigated in this study is the thermophilic iron–sulfur protein rubredoxin from *Pyrococcus furiosus* (RdPf). This organism survives in superheated deep sea vents and has attracted significant industrial and scientific attention due to its remarkable stability at elevated temperatures. RdPf is a small $\alpha + \beta$ protein (6 kDalton, 53 residues) whose structure has been the subject of many X-ray and neutron diffraction measurements.³⁸ RdPf is involved in electron transfer by means of a Fe^{3+} ion tetrahedrally coordinated to four conserved cysteine residues, located on two semiparallel loops. MD simulations were previously employed to estimate the changes in RdPf redox potential with temperature,³⁹ although the evolution of its dynamics with temperature and the connection of that dynamics to function have not been explored. RdPf is stable for days in boiling water and is one of the most thermostable proteins characterized to date.⁴⁰ Thus, this protein is of interest as a model system for investigation of fundamental questions concerning the structural, functional, and dynamical properties that provide resilience to such high temperatures. Studies for the majority of thermostable proteins report a stabilization of an enthalpic nature, leading to an increase in rigidity and compactness of the native state by virtue of their stronger inter-residue contacts, when compared to their mesophilic counterparts.⁴¹ Nevertheless, stabilization in some proteins may also be the result of entropic factors.⁴² Extreme thermal stability of most hyperthermophilic proteins causes an increase in conformational rigidity of the molecular structure;⁴³ however hydrogen exchange kinetics of RdPf reported values similar to its mesophilic counterpart over two-thirds of the amino acid sequence.⁴⁴

This article reports on computational methodologies in conjunction with a series of neutron scattering experiments to identify the harmonic, quasi-harmonic, and anharmonic motions in oxidized RdPf. The evolution of the protein dynamics from low-temperature vibrational motion to high temperature anharmonic, diffusive modes is explored by both MD simulations and QENS. A methodology for identifying those motions and residues most relevant to function is described, and a detailed picture is presented on how these motions develop with increasing temperature.

METHODS

Protein Preparation and Neutron Scattering Experiments.

Protein was purified, lyophilized, and labile hydrogen atoms exchanged for deuterium according to the procedure described in the Supporting Information (SI). The dry powder was hydrated with D_2O vapor to an H_2O equivalent water/protein mass ratio of 0.36. This hydration level is well into the range where proteins exhibit a dynamic transition.^{45,46}

Neutrons scattered by the hydrogen atoms in the sample were collected as a function of arrival time to the detector and deflection angle of the neutron trajectory. Neutrons that scattered as a result of diffusive motions give rise to a signal that is centered at zero energy transfer ($\omega = 0$) and has a width inversely proportional to the time scale of the motions. This type of scattering event is termed QENS, and its measurement typically requires relatively high instrumental energy resolution. QENS

measurements were carried out at four temperatures 200 K, 240 K, 300 K, and 325 K. The instrument resolution function $R(\omega)$ was measured at 30 K where anharmonic and diffusive motions are frozen out and fitted to a normal distribution with full width at half-maximum of 24 μeV . Additional inelastic neutron scattering (INS) measurements were made at higher momentum and energy transfers (see SI) where the spectrum is sensitive to excitations such as the boson peak. INS data were collected at temperatures of 100 K, 180 K, and 220 K. The histogram of collected neutrons versus deflection angle and arrival time was transformed to a scattered intensity versus modulus of momentum transfer, Q , and energy transfer, ω . This intensity is simply related to the symmetrized incoherent dynamic structure factor, $S(Q, \omega)$ (see references in SI). The high sensitivity of the neutron to hydrogen implies that the measured signal is dominated by the hydrogen atoms in the protein. Approximately 89% of the scattering is calculated to come from the protein hydrogen atoms, 6% from the remaining protein heavy atoms, and 5% from D_2O .

Diffusion Models. Several studies have indicated that for temperatures below T_{DT} , the quasielastic component of the structure factor is dominated by rotational motions of the methyl groups.^{25,47–49} Thus, a model describing diffusion in a circle of radius 1.03 Å passing through the three methyl hydrogens is appropriate to fit the structure factor at these temperatures. The model ($S_{\text{C}}(Q, \omega, R, D_{\text{r}})$) is characterized by a circle radius ($R = 1.03$ Å) and fitted by a rotational diffusion constant (D_{r}). For temperatures above T_{DT} , the quasielastic component of the structure factor is dominated by side-chain diffusion. Thus, a convenient model frequently employed is that of diffusion in a sphere with rigid boundaries.^{18,50} The model ($S_{\text{S}}(Q, \omega, R, D_{\text{t}})$) is fitted by a sphere radius (R) and a translational diffusion constant (D_{t}). Since not all of the hydrogen atoms undergo diffusive motions on the measured length and time scales, the intensity associated with slow or very localized, vibrational motion is captured by an additional elastic term. To account for the reduction in intensity due to localized vibrational motions, a Debye–Waller like term multiplies both the diffusive and localized terms. In principle, it would be appropriate to postulate a different $\langle u^2 \rangle$ for the two terms, but in practice the data do not allow such a separation, and this ansatz has been used previously for analyzing QENS from proteins.^{46,51–53} The two models were fit to both the experimentally measured and the MD calculated $S(Q, \omega)$:

$$S(Q, \omega) = e^{-Q^2 \langle u^2 \rangle / 3} (A_0 \delta(\omega) + A_1 S_X(Q, \omega, R, D_X)) \quad (1)$$

where A_0 is the fraction of hydrogen atoms executing slow or localized vibrational motion and A_1 represents the fraction of hydrogen atoms executing diffusive motion on the time scale of the simulation and experiment. S_X stands for either the circle (S_{C}) or sphere (S_{S}) model, and D_X represents the rotational or translational diffusion coefficient, depending on the model employed. The resolution function of the simulation was constructed to be that of the experiment (24 μeV full-width at half-maximum). The relevant resolution function was convoluted with the model of eq 1 and fit to both the experimental and calculated spectra. Spectra at all Q -values were fit simultaneously. The experimental spectra at the lowest two momentum transfers (0.23 and 0.33 Å^{−1}) could not be fit to this model and required an additional elastic intensity likely arising from the remnants of small angle scattering originating in the contrast between the D_2O hydration water and the protein.

Computational Model Preparation and Simulation Protocol.

MD simulations were performed at seven temperatures from 100 to 360 K. The starting coordinates of oxidized RdPf were based on a high resolution crystal structure previously determined by our group using a combination of X-ray and neutron diffraction.^{38,54} Structure preparation and MD simulations were performed with the AMBER 9.0 package and *parm98* force field.⁵⁵ The suitability of *parm98* for reproducing protein motions has been previously verified.⁵⁶ Crystallographic hydrogen atoms were modeled with AMBER's leap module to avoid any close contacts. Histidine residues 5, 8, 38, and 41 were singly protonated, based on the hydrogen-bonding pattern found in the crystal structure. The four ionic Fe^{3+} –S bonds were modeled by a weak harmonic restraints ($r_{\text{eq}} = 2.4$ Å, $k = 25$ kcal/mol·Å²), and a neutrally charged system was obtained by the addition of 9 Na^+ ions. The protein and ions were solvated with 3626 pre-equilibrated SPC/E⁵⁷ deuterated water molecules. Bulk water simulations of the SPC/E water model indicate freezing at $T = 215$ K and normal pressure.⁵⁸ However, the water in the hydrated powders employed in the neutron scattering experiments exists in a glassy state at low temperatures. Existing studies of shear viscosity for the SPC/E water model provide some evidence regarding the validity of the model to simulate viscous water in hydrated protein powders.⁵⁹ Our SPC/E D_2O computational model features a topology and force field identical to that of the SPC/E H_2O model, the only difference being the higher mass of the deuterium atom. Protein, ions, and water comprised a box of dimensions such that the minimum distance between the protein and any side of the box was 10 Å. The actual box dimensions depended on the temperature of the particular simulation, ranging from 114 nm³ for the simulation at $T = 100$ K to 122 nm³ for the simulation at $T = 360$ K, a 7% volume increase due to thermal expansion. The system was pre-equilibrated in the NPT ensemble at 1 atm pressure and at the highest simulated temperature with a previously described protocol⁶⁰ involving a series of minimization and equilibration steps. The final equilibrated conformation served as a starting conformation both for the subsequent production phase and for the equilibration process at the next lower temperature. Thus, the starting conformation for the production phase at the lowest temperature simulated was the result of a series of cooling steps, each step consisting in turn of a set of minimizations and equilibrations. All simulations in the production phase were carried out in the NVE ensemble. Production phases lasted 1 ns each, with a 1 fs integration time step. Conformations were collected every 20 fs for a total of 50 000 conformations per simulation. Simulations were carried out in the temperature range 100–360 K using this protocol. No bonds in the simulations were constrained, including bonds involving hydrogen atoms.

Mean Square Displacements (MSD). The time-dependent MSD for each hydrogen atom, as well as their average, was calculated directly from the MD trajectories:

$$\text{MSD}_i(t) = \langle |\vec{r}_i(t_0) - \vec{r}_i(t_0 + t)|^2 \rangle_{t_0}, \text{MSD}(t) = \frac{1}{N} \sum_{i=1}^N \text{MSD}_i(t) \quad (2)$$

where i denotes a particular hydrogen atom, $\vec{r}_i(t)$ is the position vector of atom i , and t_0 denotes a particular recorded conformation. The $\text{MSD}(t \rightarrow \infty)$ is just twice⁴⁹ the $\langle u^2 \rangle$ of eq 1 if all hydrogen atoms were executing localized vibrations, which, apart from methyl rotations as discussed later, is the case at low temperature.

Principal Component Analysis (PCA). PCA is a well-established method to study collective motions, particularly in proteins.^{12,56} PCA may be interpreted geometrically as the linear transformation of coordinates by rescaling and rotation⁶¹ to diagonalize the mass-weighted covariance matrix. Eigenvectors (modes) can then be interpreted as uncorrelated collective motions of the protein. A physical interpretation consists of a simplification of the potential energy landscape by use of a set of harmonic potentials, or springs, giving rise to the same second moments in the observed probability distribution of coordinates.⁶² In this interpretation, eigenvectors are harmonic motions having the frequencies of the springs. By projecting the trajectory coordinates onto a particular mode coordinate, one can also compute a MSD(*t*) for each mode.

Harmonicity of the Modes. The goodness-of-fit χ^2 value between the distribution of the mode coordinate and a fit to a normal distribution can be taken as a measure of the deviation from harmonicity; higher values of χ^2 indicate greater deviations from harmonic behavior. As temperature decreases, the number of harmonic modes is expected to increase because the probability of large thermal fluctuations driving diffusive motions becomes small. Thus, it is reasonable to define a χ^2 cutoff value characterizing mode harmonicity based on results at the lowest simulation temperature of 100 K where the number of harmonic modes will be greater than at any higher temperature. The average and standard deviation of χ^2 at 100 K is $2.0 \times 10^{-3} \pm 1.0 \times 10^{-3}$. In this study, a mode will be labeled as harmonic if its χ^2 is lower than the low temperature baseline average plus two standard deviations, that is, $\chi^2 \leq 4.0 \times 10^{-3}$. A mode is deemed anharmonic if its coordinate distribution shows two or more peaks, or if the distribution contains long tails that cannot be adequately fit by a normal distribution. These anharmonic modes have the highest values of χ^2 , typically $\chi^2 > 1.0 \times 10^{-2}$. Modes with χ^2 greater than or equal to this value will be labeled anharmonic. Last, quasi-harmonic modes are defined as modes that cannot be labeled as either harmonic or anharmonic and have χ^2 values between 4.0×10^{-3} and 1.0×10^{-2} .

Electrostatic Fluctuations. In any given mode, the Fe³⁺ ion moves in a particular direction with a determined amplitude. Modes displacing the Fe³⁺ ion in directions with sufficient amplitude to facilitate reduction are expected to be most relevant to RdPf function. Mean field electrostatic fluctuations (φ) on the Fe³⁺ ion site can be estimated as the work done by the average electrostatic force along the vector displacement for any given mode:

$$\varphi_i = \delta q_i \vec{f}_{av} \cdot \vec{e}_i \quad (3)$$

where δq_i is the standard deviation of the coordinate distribution for mode i , \vec{e}_i is the vector displacement of the Fe³⁺ ion for such mode, and \vec{f}_{av} is the electrostatic force acting on the ion, averaged over 5×10^3 conformations. Modes with the highest φ values are expected to be those most important for RdPf function, as they maximize the electrostatic fluctuations experienced by the Fe³⁺ ion.

RESULTS AND DISCUSSION

Diffusive Motions Derived from QENS and MD. The protein motions obtained from computational simulations were compared to data obtained using neutron scattering experiments. For a more direct comparison with the neutron scattering data, which

is heavily weighted by the signal from the hydrogen atoms, the calculated dynamic structure factor was generated from the MD simulation trajectories only for the hydrogen atoms via eq S1 in the SI. In the vicinity of the elastic peak ($\omega = 0$) where diffusive motions are first manifested, $S(Q, \omega)$ was fit by the models expressed in eq 1.

Figure 1a shows the temperature evolution of the two populations of hydrogen atoms, those having diffusive motions on the time scales of the simulation and experiment (A_1) and those executing only localized vibrations (perhaps along with diffusive motions too slow to be sampled) (A_0). The simulation exhibits a more rapid increase in A_1 than seen in the experiment. The observed sudden increase in A_1 in the vicinity of T_{DT} agrees with previous experiments⁶³ and computational studies⁶⁴ that show the onset of free diffusive motions in the neighborhood of T_{DT} . Arguably, the higher hydration level of the simulations may be responsible for the higher population of protein hydrogens undergoing diffusive motions even though $S(Q, \omega)$ was generated at the same resolution. Both experiments and simulations show a more pronounced decay of the elastic intensity A_0 for temperatures above 200 K, albeit at different temperature ranges. A fit of the experimental and simulated A_0 to a logistic function (see eq S2 in SI) resulted in $T_{DT,exp} = 302 \text{ K} \pm 33 \text{ K}$ and $T_{DT,sim} = 225 \text{ K} \pm 35 \text{ K}$, respectively. Although more experimental data points would be desirable to make a more precise determination of $T_{DT,exp}$, a somewhat higher value is consistent with the lower hydration level of experiments relative to the simulations.⁶⁵ In addition, a close examination shows that, due to the limited statistics of the experimental data, the simulation has a higher sensitivity to slower diffusing hydrogen atoms when an appreciable elastic signal is present even though the resolution of the simulation was chosen to match the experimental conditions. Because both the experiment and simulation average over all hydrogen atom motions, this additional sensitivity means that the simulation will have both a lower A_0 (higher A_1) and a slower average diffusion coefficient than observed experimentally at any given temperature. At higher temperatures as all motions become more rapid the differences tend to diminish. Diffusive motions indicated below T_{DT} likely arise from rotation by some of the 20 methyl groups of the protein, in agreement with other calculations and experiments.^{25,48,66} A signature of the dynamic transition is seen in the behavior of the square root of the average squared displacement from eq 1 in Figure 1b. At temperatures below T_{DT} , $\langle u^2 \rangle^{1/2}$ increases linearly with temperature, with an abrupt increase in slope at T_{DT} . This may be an indication of an effective expansion of the protein facilitated by diffusive motion, thus providing excess volume for the more localized vibrations with an accompanying increase in amplitude. At the three highest experimental temperatures, two sets of $\langle u^2 \rangle^{1/2}$ are shown in Figure 1b. The sample was removed and then reinserted into the neutron beam between the 200 and 240 K measurements. It was noted that the energy-integrated intensities as a function of momentum transfer in $S(Q, \omega)$ changed between these two measurements and as a consequence the higher temperature intensities were rescaled to correct this difference. The dark circles at 240, 300, and 325 K are the result of fitting the corrected data, while the lighter circles at these temperatures result from fitting uncorrected data. No other parameters deviated outside their reported uncertainties due to this process.

Table 1 shows the diffusion coefficients and radii after fitting the quasi-elastic intensity to the diffusion models described in the Methods section. The large uncertainties in the experimentally

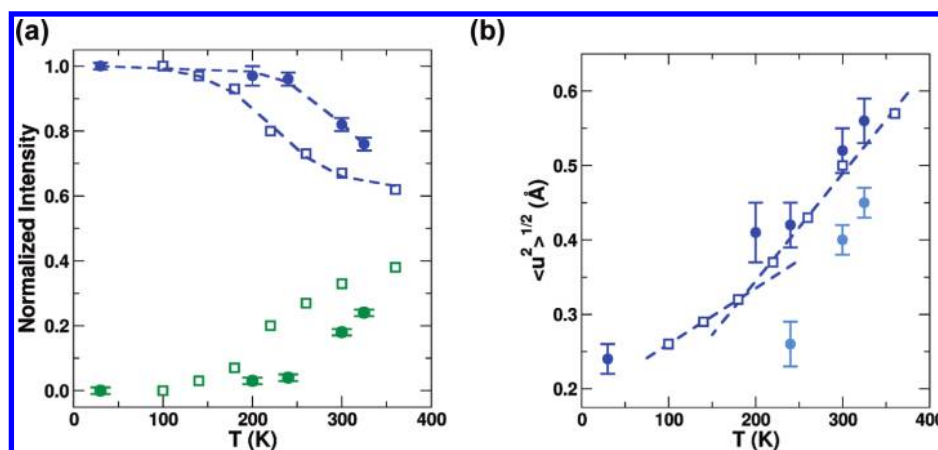


Figure 1. Fitting parameters resulting from modeling the quasielastic portions of experimental (circles) and simulated (squares) dynamic structure factors using eq 1. In plot a, blue and green symbols correspond to the fractions of elastic (A_0) and quasielastic (A_1) intensities, respectively. Fits of experimental and simulated elastic intensities to a logistics function are depicted as dashed lines, with corresponding dynamical transition temperatures of $T_{DT,exp} = 302 \text{ K} \pm 33 \text{ K}$ and $T_{DT,sim} = 225 \text{ K} \pm 35 \text{ K}$. Plot b indicates the Debye–Waller factor for experiments (circles) and simulations (squares). Circles in light blue at 240, 300, and 325 K were obtained from uncorrected experimental data, while circles in blue at these temperatures were derived after corrections as described in the text. Two linear fits of simulated $\langle u^2 \rangle^{1/2}$ below and above T_{DT} are indicated with dashed lines. Error bars indicate one standard deviation.

Table 1. Parameters from Fits to the Quasi-Elastic Region of the Dynamic Structure Factors Measured by Neutron Scattering and Calculated from Trajectories Generated by MD Simulations

experiment				simulation			
$T \text{ (K)}$	$D_t \text{ (} 10^{-5} \text{ cm}^2/\text{s})$	$R \text{ (Å)}$	$D_r \text{ (} 10^9 \text{ rad/s)}$	$T \text{ (K)}$	$D_t \text{ (} 10^{-5} \text{ cm}^2/\text{s})$	$R \text{ (Å)}$	$D_r \text{ (} 10^9 \text{ rad/s)}$
-	-	-	-	140	-	1.03	5.6
-	-	-	-	180	-	1.03	13
200	-	1.03	51 ± 41	220	-	1.03	35
240	0.62 ± 0.21	1.8 ± 0.4	-	260	0.23	1.6	-
300	0.49 ± 0.04	2.1 ± 0.1	-	300	0.26	1.7	-
325	0.61 ± 0.03	2.2 ± 0.1	-	360	0.51	1.8	-

determined values at low temperatures are a consequence of the very small fraction of hydrogen atoms participating in this motion and the correspondingly weak signal. Regardless of the model employed, diffusion coefficients corresponding to experiments are higher than those corresponding to the simulations. We recall, however, that the population of hydrogen atoms undergoing diffusive motions (parameter A_1 in Figure 1a) is smaller in experiments than in simulation with the simulations having a higher sensitivity to slower motions. Thus the average diffusion coefficient in the experiment is faster than that of the simulation. The disparity is enhanced at lower temperatures, with a concomitant decrease in the amplitude of solvent diffusive motions. This raises the question of whether cooperative effects in the bulk of the simulated solvent inhibit the faster diffusion observed in the experiments having a lower hydration level.

There is qualitative agreement between radii (R) obtained from experiments and simulations, with experiment-derived R consistently greater ($\sim 20\%$ more) than simulation-derived R . This result is expected because hydrogens in experiments undergoing diffusive motions will be preferentially located in regions of the protein surface that are hydrated. These regions correspond to loops, where there is a higher concentration of hydrophilic residues, and loops are the most flexible regions of a protein. In the simulations, however, there is a higher population of hydrogens

undergoing diffusive motions at any given temperature, and a fraction of these will be located in elements of secondary structure like helices and strands, less flexible than the loops. Both experiment and simulation determine an average radius for all diffusing hydrogen atoms, but the simulation-derived radius will include a higher contribution from hydrogen atoms located in the less flexible regions of the protein. Hence, the reported diffusion radius for the simulation should be smaller than the reported radius for the experiments. The 300 K value of $R = 2.1 \pm 0.1 \text{ Å}$ measured here for rubredoxin is somewhat smaller than that reported for lysozyme⁴⁶ (2.7 Å), aspartate transcarbamylase⁵² (2.7 Å), and dihydrofolate reductase⁵¹ (2.5 Å). This is likely a reflection of the more tightly bonded nature of rubredoxin, which may also be largely responsible for the high thermal stability of this protein.

Fe³⁺ Electrostatic Interactions. The electrostatic force exerted on the Fe³⁺ ion was calculated for every stored protein conformation as temperature was gradually increased from 100 to 360 K. Although the force components show large fluctuations, there is a net average electrostatic force that displaces the Fe³⁺ ion from its coordinated position. Interestingly, the direction of this average force flips 180° upon crossing T_{DT} . Below T_{DT} , the net electrostatic force tends to point toward the cleft left by Ile7 and Cys41. At temperatures above T_{DT} , the force tends to

point toward the cleft left by Ile40 and Tyr10 (Figure 2), as anharmonic modes with significant atomic displacements are activated. Ile7 and Ile40 are located at the RdPf active site and have been identified as key residues that modulate the Fe^{3+} redox potential. These residues, along with Cys8 and Cys41, shield the Fe^{3+} ion from the solvent and provide backbone hydrogens (from the N–H groups) to the Fe^{3+} -coordinated sulfur atoms.⁶⁷

Since the Fe^{3+} ion is isolated from the solvent, its motion should be correlated with that of the surrounding protein atoms. PCA analysis is a useful tool to study atomic correlations, and the resulting modes may provide a useful description of the possible relationship between collective motions and

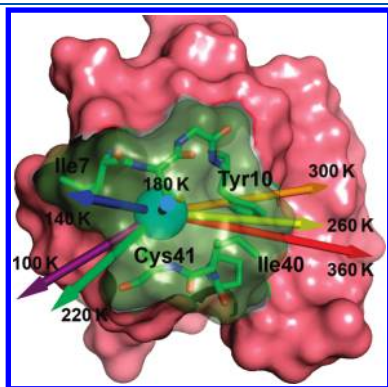


Figure 2. Average electrostatic force vectors on the Fe^{3+} computed at different temperatures. Below T_{DT} , the average force lies preferentially in-between Ile7 and Cys41. Above T_{DT} , the force direction lies preferentially in-between Ile40 and Tyr10. The switch in the force direction is directly related to the activation of diffusive motions with temperature.

electrostatic fluctuations (ϕ) experienced by the Fe^{3+} ion. As the temperature is raised from 100 to 360 K, modal electrostatic fluctuations increase by one order of magnitude for those modes showing the highest ϕ values, mainly due to an increase in the magnitude of atomic fluctuations enabled by diffusive motions (Figure 3). Electrostatic fluctuations were also studied at the active site of the metalloprotein plastocyanin,⁶⁸ and the authors observed a marked increase in these fluctuations accompanying desolvation of exposed hydrophobic residues at elevated temperatures. At 360 K, close to the optimal growth temperature of *P. furiosus*, modes 2, 6, and 7 have the largest ϕ values, which are significantly greater (57%) than mode 10, the next strongest mode (Figure 3, $T = 360$ K). These three modes are all anharmonic and may be the most relevant ones for Fe^{3+} reduction at 360 K as they impart the strongest electrostatic fluctuations on the Fe^{3+} ion and may also facilitate access of the solvent to its location. Residue displacements along each mode were calculated based on the associated mode eigenvalue, that is, the MSD, and the direction specified by the mode eigenvector. Figure 4 depicts the motions of important residues in three important modes. Mode 2 (Figure 4a) shows 3 Å displacements of the segment Lys6-Ile7 from the relatively static residues Ala43 and Glu47, providing a cavity that allows water to approach Fe^{3+} . The Lys6 amino group is observed to oscillate between the carboxylic group of Glu49 at maximum cavity opening and the backbone oxygen of Ser46 at minimum cavity opening. Mode 2 also shows 1 Å displacements of Ile40 away from Tyr10. Mode 6 (Figure 4b) shows similar motions in the neighborhood of the active site, albeit with smaller amplitudes, 2 Å displacements of Ile7 from Glu47, and 0.3 Å displacements between Ile40 and Tyr10. Finally, mode 7

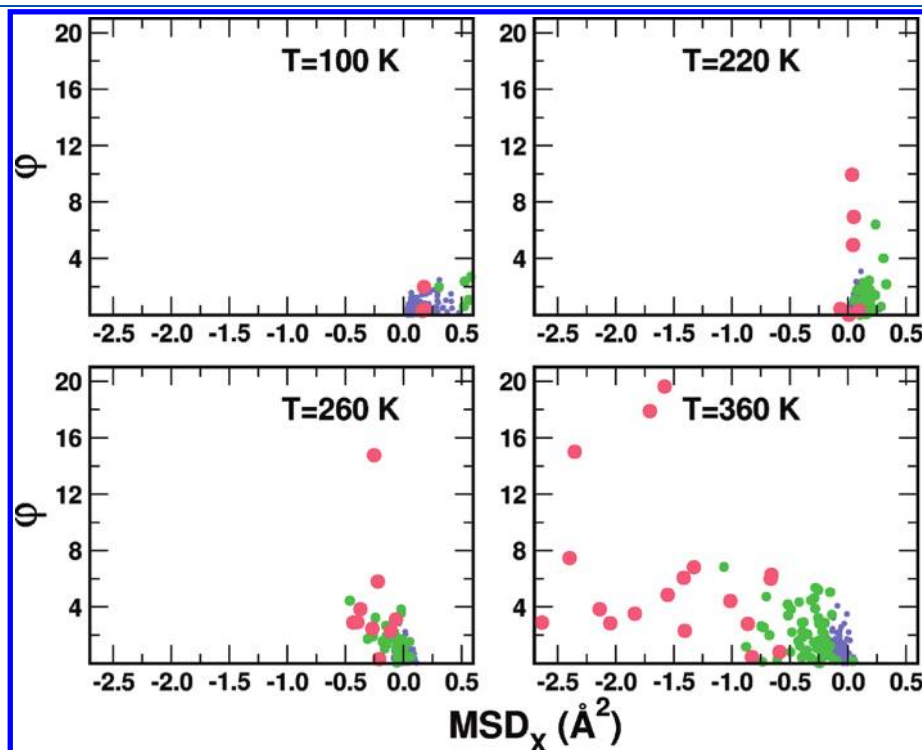


Figure 3. Contribution of RdPf motions to electrostatic fluctuations: Electrostatic fluctuations (ϕ) on the Fe^{3+} ion imparted by different modes are depicted as a function of MSD_x . Harmonic, quasi-harmonic, and anharmonic modes are shown as blue, green, and red filled circles, respectively. Above T_{DT} , only a fraction of the harmonic modes retain positive MSD_x values and small ϕ values, while anharmonic modes show negative MSD_x values and high ϕ values.

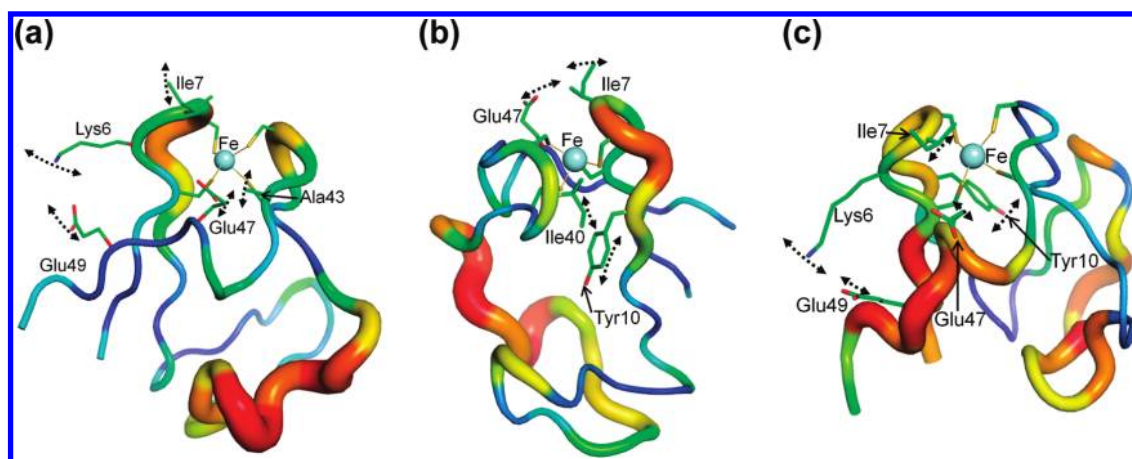


Figure 4. Three modes with the largest contributions to the electrostatic fluctuations at the Fe^{3+} site for $T = 360$ K. Displacements of residues relevant to rubredoxin function are shown for each mode in panels a–c. Mode number 2 is depicted in panel a, mode 6 in panel b, and mode 7 in panel c.

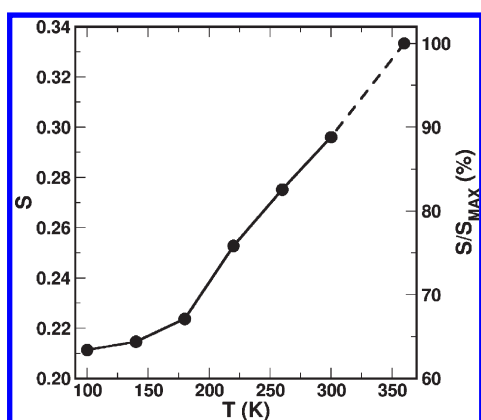


Figure 5. Similarity measure S between the three modes with the highest electrostatic fluctuations and the three analogous modes calculated at 360 K, whose value is S_{MAX} . A monotonous increase of S is observed, convergent toward S_{MAX} .

(Figure 4c) shows 3 Å displacements between Ile7 and Glu47, as well as 0.5 Å displacements between Tyr10 and Ile40. Interestingly, mode 7 shows motions of the Lys6 side chain such that its amino group oscillates between the carboxylic groups of Gly49 (native interaction) and Glu47. The alternative electrostatic interactions that Lys6 can make with Ser46, Glu47, and Glu49 may be a driving force for fluctuations in the Lys6-Ile7 segment that enable water proximity to Fe^{3+} . Both Ile6 and Glu47 residues have already been identified to lower the reorganization free energy of the active site in mesophilic rubredoxin from *Clostridium pasteurianum*.⁶⁷

One means of identifying the temperature evolution of functionally relevant motions is to define a similarity metric comparing these three significant high-temperature modes to the top three modes ranked by φ at other temperatures

$$S(T) = \frac{1}{3^2} \sum_{i=1}^3 \sum_{j=1}^3 \bar{Q}_i(T) \cdot \bar{Q}_j(T_{\text{max}}) \quad (4)$$

where $\bar{Q}_i(T)$ is the normalized eigenvector of mode i at temperature T . As shown in Figure 5, $S(T)$ converges linearly to its maximum value of 1/3 as T approaches 360 K. At temperatures above T_{DT} , modes with the highest φ are anharmonic, while

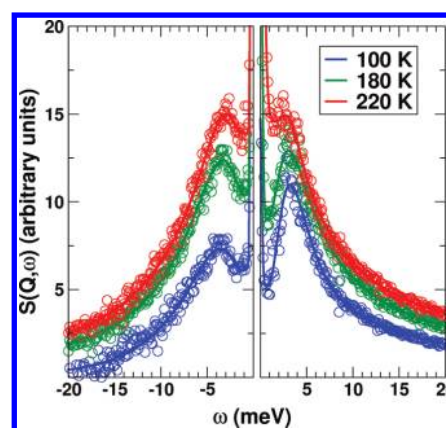


Figure 6. Measured (left panel) and computed (right panel) dynamic structure factors for RdPf. Inelastic neutron scattering was used to measure the dynamic structure factor in neutron energy loss as the left panel, while the right panel was calculated from atomic displacements from MD simulations. The boson peak is visible between 0 and 5 meV. Although the absolute units of $S(Q, \omega)$ are arbitrary, the data in individual panels are scaled identically relative to each other, and the relative intensities are meaningful quantities.

below T_{DT} , modes with the highest φ are quasi-harmonic as seen in Figure 4. This change in the character of the protein motion is manifested as a sudden variation in the slope of $S(T)$ in the vicinity of T_{DT} . The types of motion most relevant to function at 360 K begin to arise at temperatures near T_{DT} , change the direction of the average electrostatic force experienced by the Fe^{3+} , and couple to a dramatic increase in the magnitude of the electrostatic fluctuations.

Boson Peak Derived from INS and MD. The dynamic structure factors measured experimentally by inelastic neutron scattering (INS) and calculated from the MD simulation hydrogen atom trajectories are shown in Figure 6 at temperatures of 100, 180, and 220 K. Apart from the much sharper delineation of the boson peak in the simulated $S(Q, \omega)$ at 100 K, the experiment and simulation exhibit both similar response and trends. The spectra were fit with a model consisting of a Gaussian, representing elastic scattering at $\omega = 0$, a Lorentzian also centered at $\omega = 0$ representing diffusive motions, a log-normal distribution representing the boson peak, and a constant background term. The

Table 2. Boson Peak Fits to Log-Normal Distribution^a

T (K)	experimental		computational	
	ω_m (meV)	A	ω_m (meV)	A
100	4.4 ± 0.3	1.0 ± 0.16	3.3	1
180	4.1 ± 0.2	0.75 ± 0.08	3.2	0.77
220	3.9 ± 0.1	0.52 ± 0.04	3.3	0.21

^a ω_m = energy transfer of maximum peak intensity, and A = peak area (arbitrary units) scaled to 100 K results.

log-normal distribution is built into the standard DAVE analysis package,⁶⁹ and this distribution has been previously used to characterize the boson peak.³³

The location of the boson peak maximum (ω_m) and area relative to 100 K (A) are given in Table 2. The experimental data exhibits a $\sim 30\%$ broader peak width along with a $\sim 30\%$ greater ω_m relative to the MD simulation. This difference has been previously addressed in other studies that compared computed and experimental structure factors.^{70,71} One possible source of the disparity is the difference in experimental and computational environments. The experimental system is a powder hydrated with D₂O to $h = 0.36$ which certainly has protein–protein contacts, while the simulation system is composed of a single protein fully immersed in D₂O. The addition of protein–protein interactions and a lower hydration level have been observed to shift the boson peak toward higher and lower frequencies, respectively,^{70,72} suggesting that protein–protein interactions have a stronger effect than hydration on ω_m . An alternative possibility is that the force fields used in the simulation are soft relative to the real interatomic interactions. This hypothesis was challenged in a recent study which also pointed out that inclusion of protein–protein interactions results in a broadening of the boson peak relative to that calculated from a simulation of a single protein.⁷¹ The presence of protein–protein contacts appear to be the likely cause of the 30% broader boson peak and the shift of ω_m observed in the present experiment relative to the MD simulation.

As temperature is increased, the boson peak decreases in intensity and narrows in width for both experiment and simulation as a consequence of the decreasing population of hydrogens participating in low-frequency vibrational motions. Due to the higher hydration level of the MD simulations, a higher population of hydrogens participates of the low-frequency vibrations and gives rise to a bigger boson peak signal at 100 K, as compared to the experiments (Figure 6). When the temperature rises above T_{DT} , a majority of hydrogens switch from vibrational to diffusive motions, hence the dramatic decrease in the simulated boson peak intensity in going from 180 to 220 K.

As measured by INS, the location of the boson peak maximum shifts from 4.4 to 3.9 meV as the temperature increases from 100 to 220 K. This shift in ω_m with temperature has also been observed in lysozyme,⁷³ myoglobin,^{31,73} and α -amylase.⁴⁵ Diehl et al. proposed that water coupled to librations of surface polar side chains in lysozyme⁷³ along with a temperature increase would activate hydrogen bond flips and decrease the overall strength of protein–water hydrogen bonds. The resulting effective softer potential would lead to librations of increased amplitude and lower frequency. However, the present simulations indicate that the hydrogen atoms of the surface hydrophobic residues, not the polar ones, and those located in the aromatic

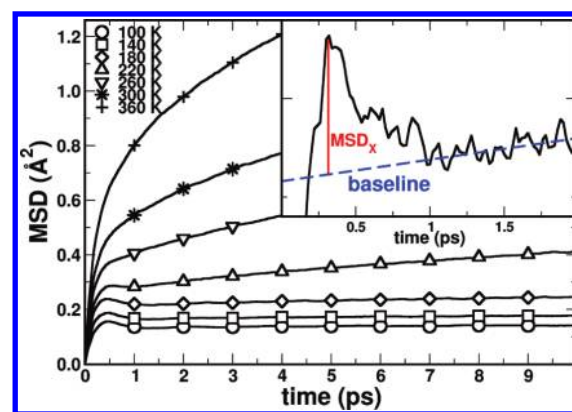


Figure 7. Time and temperature dependence of mean square displacement (MSD) for RdPf hydrogen atoms. Inset: definition of MSD_x (vertical red line) as the difference between the local maximum of the MSD plot and the baseline (blue line). MSD_x is visible in the main panel at temperatures below 260 K.

rings of buried residues make the largest contributions to the boson peak intensity at temperatures below T_{DT} . Water tends to form tight ordered structures around hydrophobic molecules at low temperatures.⁷⁴ As the temperature is increased, these water cages will tend to fluctuate and expand, providing a lowered confinement of the hydrophobic residues, thus resulting in a softer effective potential, finally shifting the boson peak to lower energy transfers. This interpretation is reminiscent of that of Joti et al.,³⁶ who assigned the origin of the boson peak to librations of protein hydrogen atoms subject to an energy landscape sculpted by a structured hydration shell.

Atomic Fluctuations and Connection to Boson Peak. MD simulations indicate that RdPf exhibits significant changes in the nature of its internal motions as temperature is increased. A close examination of the $MSD(t)$ averaged over all hydrogen atoms and shown in Figure 7 gives further insight in to the change in dynamics that occurs at T_{DT} (about 220 K). Beginning with the intermediate structure factor, $I(Q, t)$, its Taylor expansion in $Q\delta r(t)$ up to second order is directly related to $MSD(t)$:

$$I \sim \frac{1}{N} \sum_{i=1}^N \frac{\sin(Q\delta r)}{Q\delta r} = 1 - \frac{Q^2}{6N} \sum_{i=1}^N \langle \delta r^2 \rangle + O^3(Q\delta r) = 1 - \frac{Q^2}{6} MSD + O^3(Q\delta r) \Rightarrow S = F\{I\} \sim \delta(\omega) - \frac{Q^2}{6} F\{MSD\} \quad (5)$$

Equation 5 relates the Fourier transform of MSD to the dynamic structure factor, S . Thus, the excess MSD over a pure diffusion model in the 0–1 ps time range (see inset of Figure 7) leads to the excess scattering of the dynamic structure factor observed in the 1–10 meV range (boson peak). The excess MSD (MSD_x) for hydrogen atom “ i ” is derived from the $MSD_i(t)$ plot as follows: (a) find the time t_m for which $MSD_i(t_m)$ is the absolute maximum in the 0–1 ps time range (inset of Figure 7); (b) take the difference between $MSD_i(t_m)$ and the baseline evaluated at t_m . The baseline is obtained from a linear fit to the diffusion regime observed for times $\gg 1$ ps. Hydrogen atoms with large MSD_x will have a greater contribution to $S(Q, \omega)$ in the $\omega = 1$ –10 meV range, where the boson peak signal is located, than those hydrogen atoms with smaller MSD_x . The physical origin of MSD_x lies in the 2–5 meV atomic vibrations that lose coherence in a time scale shorter than the period of oscillation. The

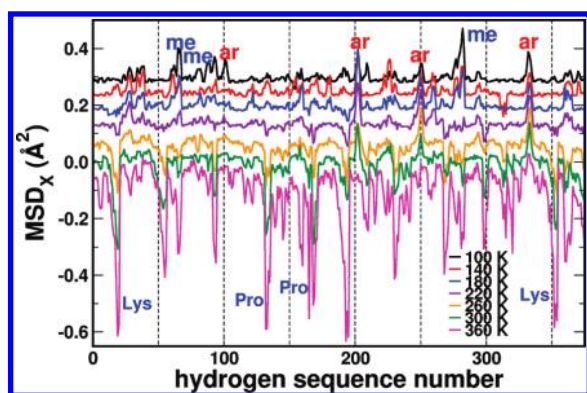


Figure 8. MSD_x profiles of RdPf hydrogen atoms in the 100–300 K range. For better visualization, offsets in the Y-axis have been applied. Peaks labeled me and ar identify the strongest peaks at 100 K and indicate hydrogen atoms belonging to methyl groups of Ile7, Ile11, and Ile40 or aromatic rings of Tyr12, Phe29, Trp36, and Phe48. Color codes in letters are blue for solvent exposed residues and red for aromatic residues buried in the interior of the protein. Lysine and proline are solvent-exposed residues. Their strong negative character implies that these residues exhibit highly diffusive motions at 300 K.

connection between these short-lived coherent vibrations and the boson peak has been implicitly noted in prior work.⁶⁶ The outlined procedure to calculate atomic MSD_x values was also employed to compute the MSD_x value from the $\text{MSD}(t)$ plot of each mode coordinate. The resulting values allow for a ranking of the modes according to their contribution to the boson peak signal. At the onset of diffusive motions above T_{DT} , this procedure results in negative MSD_x values for those modes with null contribution to the boson peak. Thus, the evaluation of this quantity provides a means of tracking the evolution of the protein dynamic behavior, from localized vibrations to truly diffusive motion.

Regardless of temperature, $\text{MSD}(t)$ shows a linear behavior for $t > 1$ ps (Figure 7). At temperatures below T_{DT} , the $\text{MSD}(t)$ for $t > 1$ ps is nearly constant, indicative of a localized non-diffusive regime. The asymptotic value of $\text{MSD}^2(t)$ for the three lowest temperatures 100, 140, and 180 K are 0.11, 0.13, and 0.25 \AA^2 , respectively. These values are approximately twice the $\langle u^2 \rangle$ determined by the fits of the MD quasi-elastic spectra (0.13, 0.16, and 0.21 \AA^2). The $\text{MSD}(t)$ presents a maximum at shorter times ($t \approx 0.5$ ps), from which MSD_x can be determined. A maximum in the time-dependent mean square displacement for $t \approx 0.5$ ps has been previously observed in MD simulations of a crystalline alanine dipeptide.⁶⁶ Due to the homogeneity of that crystalline system, the maximum could be understood as the first wave-quarter of the dominant low-frequency vibration observed in the $\text{MSD}(t)$ plot. Thus, MSD_x could be interpreted as the amplitude of low-frequency vibrations providing a connection between MSD_x and the boson peak, which arises from an excess of low-frequencies excitations over the Debye model describing vibrations in a crystal. Turning to RdPf, no obvious vibrational component can be discerned as persistent oscillations in the $\text{MSD}(t)$ of Figure 7, the reason being the high heterogeneity of the environments surrounding the different hydrogens of RdPf, as compared, for instance, to crystalline alanine dipeptide. Different hydrogens in RdPf have slightly different frequencies of vibrations that rapidly lose any coherence canceling each other for $t > 1$ ps, leaving only the first wave-quarter when the

vibrations are relatively in-phase. The vibration can be better discerned in the $\text{MSD}(t)$ of individual hydrogens or of particular collective modes as projected using PCA. Thus, $\text{MSD}(t)$ was computed, and a corresponding MSD_x was obtained for each hydrogen atom and mode.

As depicted in Figure 8, MSD_x profiles of RdPf hydrogen atoms at different temperatures demonstrate a wide range of MSD_x values. At 100 K, hydrogen atoms with the highest MSD_x are located in the solvent-exposed methyl groups of Ile residues (Ile7, Ile11, and Ile40) as well as in the rings of buried aromatic amino acids (Tyr12, Phe29, Trp36, and Phe48). These atoms provide the strongest contributions to the boson peak at this temperature. A previous simulation study of hydrated ribonuclease A also observed contributions to the boson peak from hydrogen atoms in buried residues and from those in surface residues.⁷⁵ Two of noted residues, Ile7 and Ile40, have been implicated in function and are here shown to regulate the direction of the average electrostatic force acting and the strength of the electrostatic fluctuations on the Fe^{3+} atom. Moderate MSD_x are observed in hydrogen atoms located in buried methyl groups. This observation suggests that a minimal amount of free volume may be necessary for the onset of significant amplitude low-frequency vibrations. Finally, the hydrogen atoms with lowest MSD_x are located in the side chains of surface charged and polar amino acids (Asp13, Glu14, Asp18, Pro33, and Lys50) for which vibrations are damped due to strong interactions with the water shell molecules.

At temperatures greater than T_{DT} , hydrogen atoms with the highest MSD_x are located in the protein core (Tyr12, Phe29, Trp36, and Phe48) and in Val37. Hydrogen atoms in the methyl groups of the Ile residues that had shown the largest MSD_x at low temperatures no longer exhibit significant MSD_x above T_{DT} . The lowest MSD_x values correspond to atoms in solvent-exposed Lys and Pro residues (Lys2, Lys6, Lys28, Pro25, Pro39, and Pro44). Paradoxically, as more free volume becomes available to the surface methyl groups as the temperature approaches T_{DT} , their respective MSD_x values diminish. To gain more insight into this behavior, a detailed examination of the onset of methyl rotations was carried out for the three groups having hydrogen atoms with the highest MSD_x at low T : Ile7, Ile11, and Ile40. At 100 K, no evidence of rotational jumps was observed, while an examination of the dihedral angles indicated that limited jump diffusion occurs at 140 K on the time scale of the simulation. At 220 K, the dihedral angle distributions indicated uniform jump diffusion for two of the groups which simultaneously exhibit negative MSD_x . At 260 K, all three groups exhibit uniform jump diffusion and exhibit a negative MSD_x , suggesting that the increase in free volume and thermal energy leads to methyl group reorientations that suppress the contribution of these atoms to the boson peak. As hydrogen atoms become engaged in truly diffusive motions, they no longer contribute any intensity to the boson peak.

At 300 K, well above T_{DT} , only hydrogen atoms located in the side chains of solvent-buried residues Trp3, Tyr12, and Phe48 show significant positive MSD_x . The motion of those hydrogen atoms is highly constrained because hydrogens in bulky aromatic side chains, in contrast to methyl hydrogens, cannot flip to an alternate iso-energetic state. These hydrogens can only undergo diffusive motion in the time scale of diffusion of the whole side chain to which they belong. In addition, this whole-side chain diffusive motion is restricted due to their location in the crowded environment of the protein core. Thus, suppression of rotation and translation degrees of motions for these residues results in a

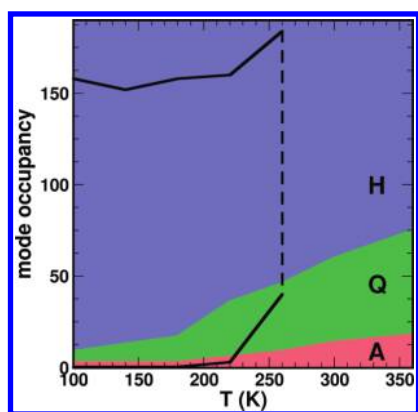


Figure 9. Decomposition of protein motions as a function of increasing temperature. In this sequence, the mode number is ordered from lowest to highest frequency. The lowest numbered modes are anharmonic (red). Going up in frequency, the next sequence of modes are quasi-harmonic (green) which show a marked increase in population upon reaching $T_{DT} \approx 220$ K. Harmonic modes are indicated in blue. Modes between the two solid black lines contribute to half the intensity of the boson peak, with the remaining intensity coming from the remaining higher numbered harmonic modes. The boson peak could not be discerned above $T = 260$ K indicated by the vertical dashed line.

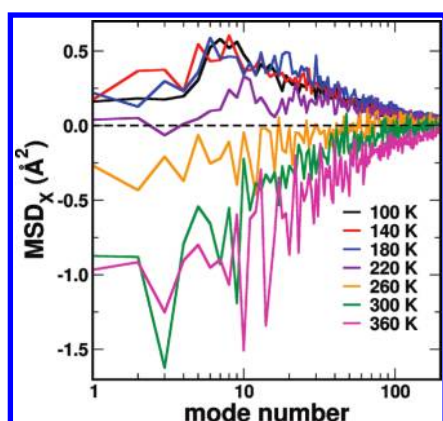


Figure 10. Modal MSD_x as a function of temperature, with high MSD_x values indicating a positive contribution of the mode to the boson peak intensity. Note that most of the MSD_x values become negative upon crossing T_{DT} from 220 to 260 K.

measurable positive contribution to the boson peak at all studied temperatures. Finally, the smallest MSD_x values are located in solvent-exposed Lys and Pro residues (Lys2, Lys6, Pro19, Pro25, Pro33, and Lys50). At 300 K, only 24 out of the 375 protein hydrogen atoms in the simulation exhibit a positive MSD_x and thus contribute to a boson peak which, however, is entirely masked by the strong quasielastic signal from diffusive motions of the remaining hydrogen atoms. The strongly negative character of MSD_x at 300 K for the solvent-exposed residues indicated in Figure 8 implies that they participate in highly diffusive motion. Thus, as temperature is gradually increased, the number of hydrogen atoms exhibiting positive MSD_x decreases, and the boson peak decreases in intensity accordingly.

Collective Motions in RdPf. While the MSD_x in Figure 8 provides information on the contribution of individual hydrogen atoms to the boson peak, the collective nature of the boson peak can be explored by calculating the MSD_x as projected onto

modes generated by a principal component analysis. PCA is a decomposition of the protein conformational fluctuations onto collective modes uncorrelated to each other which may be ranked by their corresponding effective frequency. Thus, the harmonic character of a mode becomes more pronounced with increasing mode number because modes with higher effective frequencies show a more harmonic character. Following the classification scheme described in the Methods section, the number of anharmonic modes remains very low and nearly constant below T_{DT} , then increases approximately linearly with temperature, as shown in Figure 9. In contrast, the number of quasi-harmonic modes increases linearly at all temperatures but with an abrupt change in slope when crossing T_{DT} . Because the total number of modes is constant, an increase in the number of anharmonic and quasi-harmonic modes has an associated decrease in the number of harmonic modes. Thus, harmonic and quasi-harmonic modes that contributed to the boson peak at low temperature become anharmonic, and their intensity is transferred from the boson peak to the quasi-elastic signal.

A time-dependent MSD can be computed for each mode, and the corresponding MSD_x can be determined, indicating the relevance of this particular collective motion for the boson peak signal. For temperatures below T_{DT} , a near exponential decay of MSD_x versus mode number was observed for all but the first few modes, which are quasi-harmonic (see Figure 10). Above T_{DT} , MSD_x becomes negative for anharmonic and quasi-harmonic modes, indicating that these are actually diffusive modes that will not contribute significantly to the boson peak. By iterating through the list of modes ranked by MSD_x , the contribution of the iterated modes to the simulated trajectory was removed, and the structure factor recomputed. The last structure factor so determined featured a boson peak with an intensity that was compared to that intensity when all modes were kept. The iteration was stopped, and the number of removed modes was recorded when the boson peak contained an intensity half the intensity of the original peak. The quasi-elastic signal masks the boson peak at temperatures higher than 260 K, making the calculation of the boson peak area unreliable. The resulting number of removed modes fluctuates between 140 and 160, about 6% of all modes, depending on the temperature. These results are in qualitative agreement with the study of the boson peak of myoglobin at 150 K by Kurkal-Siebert and Smith.²⁸ These authors concluded that the vast majority of the boson peak signal arose from the first 200 modes and that the first few anharmonic modes did not contribute significantly to the boson peak.

SUMMARY AND CONCLUSIONS

A combination of QENS, inelastic neutron scattering, and MD simulations has been implemented to explore changes in RdPf dynamics with temperature. At temperatures well below the dynamic transition temperature, the dynamics is characterized by harmonic motions, localized vibrations which give rise to a boson peak in the measured and calculated dynamic structure factor. As the temperature is increased to 140 K, jump diffusion of the methyl groups of solvent-exposed Ile residues begins to occur, consistent with many other experiments and simulations.^{25,48,66} At the dynamic transition temperature, a significant onset of anharmonic, diffusive modes is observed, which continues to develop and increase in number to the highest temperatures

investigated, 325 K for the experiment and 360 K for MD simulation.

A metric for determining the relative contribution of individual hydrogen atoms to the boson peak, MSD_x , has been presented. As seen in Figure 8, the sign and magnitude of the excess mean square displacement vary significantly with temperature and local environment of the hydrogen atoms. Hydrogen atoms having large and positive values of MSD_x contribute the most intensity to the boson peak. As temperature increases and these atoms participate in diffusive motions, MSD_x changes sign, and these atoms no longer contribute any intensity to the boson peak. However, other hydrogen atoms in the protein continue to exhibit positive MSD_x , and the boson peak persists to relatively high temperatures. As diffusive motions develop larger amplitude displacements, MSD_x becomes increasingly negative. Interestingly, even at the highest temperatures, MSD_x is positive for hydrogen atoms buried in the interior of the protein, and they should produce a boson peak which however is entirely masked by the strong quasi-elastic scattering associated with diffusive motions.

At the dynamic transition temperature, anharmonic motions arise in the simulated trajectories which dramatically change the direction of the average electrostatic force experienced by the Fe^{3+} ion responsible for RdPf function and significantly increase the magnitude of the electrostatic fluctuations at the Fe^{3+} site. These anharmonic modes engage two conserved surface residues (Ile7 and Ile40) located at the protein active site. Their motion continues to play a significant role in the electrostatic fluctuations experienced by the ion as temperature is increased to 360 K, close to the optimal growth temperature for *P. furiosus* (Figure 3). These modes may provide solvent accessibility to the Fe^{3+} ion, which could be a necessary intermediate step in electron transfer from a nearby molecule susceptible to oxidation. At the lowest temperature, hydrogen atoms in these residues make the strongest contribution to the boson peak, suggesting the hypothesis that determination of the residues most relevant to the boson peak may help to identify functionally important residues in other proteins.

The present study provides insights into the role of protein motions in regard to protein function. The correlation between the onset of anharmonicity and electrostatic fluctuations as well as the changes with temperature of relevant motions shed light into the proposed link between protein dynamics and function. These observations support the emerging paradigm that emphasizes *structure encodes dynamics* and together *structure-dynamics encode function*.

■ ASSOCIATED CONTENT

S Supporting Information. Details of sample preparation and neutron scattering measurements, computational modeling, and analysis methodology. This material is available free of charge via the Internet at <http://pubs.acs.org/>.

■ AUTHOR INFORMATION

Corresponding Author

*Jose M. Borreguero, Oak Ridge National Laboratory, P.O. Box 2008, MS 6164, Oak Ridge, TN 37831. Phone: (865) 241-3071. Fax: (865) 576-5491. E-mail: borreguerojm@ornl.gov. Kenneth Herwig, Oak Ridge National Laboratory, P.O. Box 2008, MS 6475, Oak Ridge, TN 37831. Phone: (865) 576-5095. Fax: (865) 241-5177. E-mail: herwigkw@ornl.gov.

■ ACKNOWLEDGMENT

We thank Dr. Arvind Ramanathan for his help in the making of Figure 5. J.M.B., J.H., and P.K.A. acknowledge the financial support by ORNL's LDRD fund. This research used resources of the National Center for Computational Sciences ORNL under the Director's Discretionary allocation (project: BIP003), which is supported by the Office of Science of the U.S. Department of Energy under Contract No. DE-AC05-00OR22725. This work utilized facilities supported in part by the National Science Foundation under Agreement No. DMR-0454672. K.W.H. acknowledges the support of the Scientific User Facilities Division, Office of Basic Energy Sciences, U.S. Department of Energy. This work also benefited from the support of the ORNL Center for Structural Molecular Biology by the Office of Biological and Environmental Research, using facilities supported by the U.S. Department of Energy and managed by UT-Battelle, LLC, under contract no. DE-AC05-00OR22725.

■ REFERENCES

- (1) Agarwal, P. K. *Microb. Cell Fact.* **2006**, *5*, 2.
- (2) Benkovic, S. J.; Hammes-Schiffer, S. *Science* **2003**, *301*, 1196–1202.
- (3) Boehr, D. D.; McElheny, D.; Dyson, H. J.; Wright, P. E. *Science* **2006**, *313*, 1638–1642.
- (4) Henzler-Wildman, K. A.; Lei, M.; Thai, V.; Kerns, S. J.; Karplus, M.; Kern, D. *Nature* **2007**, *450*, 913–916.
- (5) Klinman, J. P. *Chem. Phys. Lett.* **2009**, *471*, 179–193.
- (6) Olsson, M. H. M.; Parson, W. W.; Warshel, A. *Chem. Rev.* **2006**, *106*, 1737–1756.
- (7) Benkovic, S. J.; Hammes, G. G.; Hammes-Schiffer, S. *Biochemistry* **2008**, *47*, 3317–3321.
- (8) Eisenmesser, E. Z.; Bosco, D. A.; Akke, M.; Kern, D. *Science* **2002**, *295*, 1520–1523.
- (9) Agarwal, P. K. *J. Am. Chem. Soc.* **2005**, *127*, 15248–56.
- (10) Cameron, C. E.; Benkovic, S. J. *Biochemistry* **1997**, *36*, 15792–15800.
- (11) Bizzarri, A. R. *J. Phys.: Condens. Matter* **2004**, *16*, R83–R110.
- (12) Ramanathan, A.; Agarwal, P. K. *J. Phys. Chem. B* **2009**, *113*, 16669–16680.
- (13) Sears, V. F. *Neutron News* **1992**, *3*, 29–37.
- (14) Marshall, W.; Lovesey, S. W. *Theory of Thermal Neutron Scattering*; Oxford University Press: London, 1971; pp 7–14.
- (15) Middendorf, H. D. *Annu. Rev. Biophys. Bioeng.* **1984**, *13*, 425–451.
- (16) Gabel, F.; Bicout, D.; Lehnert, U.; Tehei, M.; Weik, M.; Zaccai, G. Q. *Rev. Biophys.* **2002**, *35*, 327–67.
- (17) Harpham, M. R.; Ladanyi, B. M.; Levinger, N. E.; Herwig, K. W. *J. Chem. Phys.* **2004**, *121*, 7855–7868.
- (18) Bee, M. *Quasielastic Neutron Scattering, Principles and Applications in Solid State Chemistry, Biology and Materials Science*, 1st ed.; Taylor & Francis: London, 1988; p 452.
- (19) Fenimore, P. W.; Frauenfelder, H.; McMahon, B. H.; Young, R. D. *Proc. Natl. Acad. Sci. U.S.A.* **2004**, *101*, 14408–14413.
- (20) Wood, K.; Frolich, A.; Paciaroni, A.; Moulin, M.; Hartlein, M.; Zaccai, G.; Tobias, D. J.; Weik, M. *J. Am. Chem. Soc.* **2008**, *130*, 4586–7.
- (21) Tarek, M.; Tobias, D. J. *Biophys. J.* **2000**, *79*, 3244–57.
- (22) Doster, W.; Busch, S.; Gaspar, A. M.; Appavou, M. S.; Wuttke, J.; Scheer, H. *Phys. Rev. Lett.* **2010**, *104*, 098101.
- (23) Daniel, R. M.; Dunn, R. V.; Finney, J. L.; Smith, J. C. *Annu. Rev. Biophys. Biomed.* **2003**, *32*, 69–92.
- (24) Loncharich, R. J.; Brooks, B. R. *J. Mol. Biol.* **1990**, *215*, 439–455.
- (25) Wood, K.; Tobias, D. J.; Kessler, B.; Gabel, F.; Oesterheld, D.; Mulder, F. A. A.; Zaccai, G.; Weik, M. *J. Am. Chem. Soc.* **2010**, *132*, 4990–4991.
- (26) Rasmussen, B. F.; Stock, A. M.; Ringe, D.; Petsko, G. A. *Nature* **1992**, *357*, 423–424.

- (27) Tsuda, M.; Govindjee, R.; Ebrey, T. G. *Biophys. J.* **1983**, *44*, 249–254.
- (28) Kurkal-Siebert, V.; Smith, J. C. *J. Am. Chem. Soc.* **2006**, *128*, 2356–2364.
- (29) Nakagawa, H.; Kataoka, M.; Joti, Y.; Kitao, A.; Shibata, K.; Tokuhisa, A.; Tsukushi, I.; Go, N. *Physica B* **2006**, *385–386*, 871–873.
- (30) Nöllmann, M.; Etchegoin, P. *Physica A* **2001**, *294*, 44–50.
- (31) Leyser, H.; Doster, W.; Diehl, M. *Phys. Rev. Lett.* **1999**, *82*, 2987.
- (32) Lubchenko, V.; Wolynes, P. G. *Annu. Rev. Phys. Chem.* **2007**, *58*, 235–266.
- (33) Boukenter, A.; Duval, E. *Philos. Mag. B* **1998**, *77*, 557–568.
- (34) Wyart, M. *Ann. Phys.-Paris* **2005**, *30*, 1.
- (35) Schulz, M. J. *Lumin.* **2004**, *110*, 418–422.
- (36) Joti, Y.; Kitao, A.; Go, N. *J. Am. Chem. Soc.* **2005**, *127*, 8705–8709.
- (37) Grigera, T. S.; Martin-Mayor, V.; Parisi, G.; Verrocchio, P. *Nature* **2003**, *422*, 289–292.
- (38) Weiss, K. L.; M., F.; Blakeley, M. P.; Myles, D. A. *Acta Crystallogr., Sect. F* **2008**, *64*, 537–540.
- (39) Swartz, P. D.; Ichiye, T. *Biochemistry* **1996**, *35*, 13772–13779.
- (40) LeMaster, D. M.; Tang, J. Z.; Paredes, D. I.; Hernandez, G. *Biophys. Chem.* **2005**, *116*, 57–65.
- (41) Berezovsky, I. N.; Shakhnovich, E. I. *Proc. Natl. Acad. Sci. U.S.A.* **2005**, *102*, 12742–12747.
- (42) Wen, X.; Patel, K. M.; Russell, B. S.; Bren, K. L. *Biochemistry* **2007**, *46*, 2537–2544.
- (43) Jaenicke, R.; Böhm, G. *Curr. Opin. Struct. Biol.* **1998**, *8*, 738–748.
- (44) Hernandez, G.; LeMaster, D. M. *Biochemistry* **2001**, *40*, 14384–14391.
- (45) Fitter, J. *Biophys. J.* **1999**, *76*, 1034–1042.
- (46) Roh, J. H.; Curtis, J. E.; Azzam, S.; Novikov, V. N.; Peral, I.; Chowdhuri, Z.; Gregory, R. B.; Sokolov, A. P. *Biophys. J.* **2006**, *91*, 2573–2588.
- (47) Roh, J. H.; Novikov, V. N.; Gregory, R. B.; Curtis, J. E.; Chowdhuri, Z.; Sokolov, A. P. *Phys. Rev. Lett.* **2005**, *95*, 038101.
- (48) Krishnan, M.; Kurkal-Siebert, V.; Smith, J. C. *J. Phys. Chem. B* **2008**, *112*, 5522–5533.
- (49) Doster, W. *Eur. Biophys. J. Biophys.* **2008**, *37*, 591–602.
- (50) Volino, F.; Dianoux, A. J. *Mol. Phys.* **1980**, *41*, 271–279.
- (51) Tehei, M.; Smith, J. C.; Monk, C.; Ollivier, J.; Oettl, M.; Kurkal, V.; Finney, J. L.; Daniel, R. M. *Biophys. J.* **2006**, *90*, 1090–1097.
- (52) Zanolli, J. M.; Herve, G.; Bellissent-Funel, M. C. *BBA-Proteins Proteom.* **2006**, *1764*, 1527–1535.
- (53) Zanolli, J. M.; Bellissent-Funel, M. C.; Parello, J. *Biophys. J.* **1999**, *76*, 2390–2411.
- (54) Gardberg, A. S.; Del Castillo, A. R.; Weiss, K. L.; Meilleur, F.; Blakeley, M. P.; Myles, D. A. *Acta Crystallogr., Sect. D* **2010**, *66*, 558–567.
- (55) Case, D. A.; Cheatham, T. E., III; Darden, T.; Gohlke, H.; Luo, R.; Merz, K. M., Jr.; Onufriev, A.; Simmerling, C.; Wang, B.; Woods, R. J. *J. Comput. Chem.* **2005**, *26*, 1668–88.
- (56) Agarwal, P. K.; Geist, A.; Gorin, A. *Biochemistry* **2004**, *43*, 10605–18.
- (57) Berendsen, H. J. C.; Grigera, J. R.; Straatsma, T. P. *J. Phys. Chem.* **1987**, *91*, 6269–6271.
- (58) Vega, C.; Abascal, J. L. F.; Sanz, E.; MacDowell, L. G.; McBride, C. *J. Phys.: Condens. Matter* **2005**, *17*, S3283–S3288.
- (59) Smith, P. E.; Vangunsteren, W. F. *Chem. Phys. Lett.* **1993**, *215*, 315–318.
- (60) Agarwal, P. K. *Proteins: Struct., Funct., Bioinf.* **2004**, *56*, 449–63.
- (61) Goldstein, H. *Classical Mechanics*, 2nd ed.; Addison-Wesley: Reading, MA, 1980; p 672.
- (62) Karplus, M.; Kushick, J. N. *Macromolecules* **1981**, *14*, 325–332.
- (63) Doster, W.; Cusack, S.; Petry, W. *Nature* **1989**, *337*, 754–756.
- (64) Smith, J.; Kuczera, K.; Karplus, M. *Proc. Natl. Acad. Sci. U.S.A.* **1990**, *87*, 1601–1605.
- (65) Paciaroni, A.; Cinelli, S.; Onori, G. *Biophys. J.* **2002**, *83*, 1157–1164.
- (66) Kneller, G. R.; Doster, W.; Settles, M.; Cusack, S.; Smith, J. C. *J. Chem. Phys.* **1992**, *97*, 8864–8879.
- (67) Sulpizi, M.; Raugei, S.; VandeVondele, J.; Carloni, P.; Sprik, M. *J. Phys. Chem. B* **2007**, *111*, 3969–3976.
- (68) LeBard, D. N.; Matyushov, D. V. *Phys. Rev. E* **2008**, *78*, 061901–9.
- (69) Azuah, R. T.; Kneller, L. R.; Qiu, Y.; Tregenna-Piggott, P. L. W.; Brown, C. M.; Copley, J. R. D.; Dimeo, R. M. *J. Res. Natl. Inst. Stand.* **2009**, *114*, 341–358.
- (70) Tarek, M.; Martyna, G. J.; Tobias, D. J. *J. Am. Chem. Soc.* **2000**, *122*, 10450–10451.
- (71) Joti, Y.; Nakagawa, H.; Kataoka, M.; Kitao, A. *Biophys. J.* **2008**, *94*, 4435–43.
- (72) Nakagawa, H.; Joti, Y.; Kitao, A.; Kataoka, M. *Biophys. J.* **2008**, *95*, 2916–2923.
- (73) Diehl, M.; Doster, W.; Petry, W.; Schober, H. *Biophys. J.* **1997**, *73*, 2726–2732.
- (74) Teeter, M. M. *The water structure surrounding proteins*; AAAS: Washington, DC, 1990; pp 44–54.
- (75) Tarek, M.; Tobias, D. J. *J. Chem. Phys.* **2001**, *115*, 1607–1612.